CHEMISTRY OF MATERIALS

Article

pubs.acs.org/cm

Photoinduced Topotactic Growth of Bismuth Nanoparticles from Bulk $SrBi_2Ta_2O_9$

Yingxuan Li,[†] Ling Zang,[§] Yan Li,[†] Yun Liu,[⊥] Chunyan Liu,[⊥] Ying Zhang,[†,‡] Hongquan He,[†,‡] and Chuanyi Wang*,[†]

[†]Laboratory of Eco-Materials and Sustainable Technology (LEMST), Xinjiang Technical Institute of Physics and Chemistry; Key Laboratory of Functional Materials and Devices for Special Environments, Chinese Academy of Sciences, Urumqi, Xinjiang 830011, China

[‡]University of Chinese Academy of Sciences, Beijing 100049, P.R. China

[§]Department of Materials Science and Engineering, The University of Utah, Salt Lake City, Utah 84108, United States

[⊥]Key Laboratory of Photochemical Conversion and Optoelectronic Materials, Technical Institute of Physics and Chemistry, Chinese Academy of Sciences, Beijing 100190, China

Supporting Information

ABSTRACT: In situ growth of bismuth (Bi) nanoparticles on bulk $SrBi_2Ta_2O_9$ (SBT) platelet is achieved by UV light illumination of SBT in aqueous glucose solutions. Interestingly, the as-produced Bi nanoparticles (NPs) are uniformly oriented with the epitaxial relationship of $[001]_{Bi}//[110]_{SBT}$, appearing as meso-single-crystal phase despite spatial separation between the NPs. Systematic investigations indicate that Bi(III) at the $(110)_{SBT}$ plane is topotactically reduced by photogenerated electrons, producing Bi atoms serving as nucleation seeds oriented from the (003) plane. Further growth of these oriented nuclei leads to formation of Bi NPs arranged laterally in mesocrystalline superstructure. The reported finding presents a simple, environmentally friendly approach toward preparation of highly organized, surface supported metal NPs through direct photoreduction of bulk metal oxides.

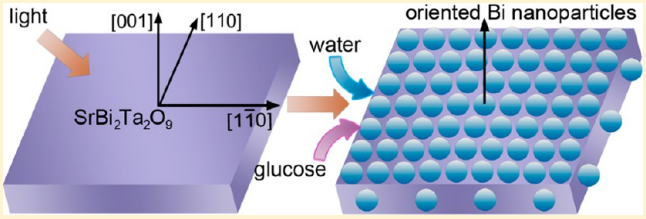

KEYWORDS: *Bi nanoparticles, $SrBi_2Ta_2O_9$, photoreduction, oriented growth*

INTRODUCTION

Metal nanoparticles (NPs) have attracted enormous attention due to their unique properties and broad applications. Various methods, via solution-phase or vapor-phase, have been developed to prepare metal NPs.[1] However, preparation of metal NPs by direct reduction of bulk metal oxides at ambient temperature remains a challenge, due to the homogeneity of bulk oxides[2] and the intrinsically slow mass transfer between the solid reactants and products in most solid-state reactions.[3] Although Cu NPs were fabricated by electroreduction of CuO at room temperature, the starting material CuO was also particulate in the same nanometer size, rather than bulk phase.[4]

Among all the methods, preparing metal NPs via photoreduction is particularly promising because it can be operated under ambient condition, and the only energy consumed is light. Although metal oxide-based photochemistry has been a topic of intensive research since 1972,[5] the direct photoreduction of bulk oxides to nanoparticulate metals is rarely reported. By means of photocatalytic reduction, surface supported transition metal NPs, such as Au, Ag, and Pt, can be produced onto the semiconductor catalysts,[6] though metal salts must be provided as the source reagent, and it is usually difficult to achieve a dense and uniform dispersion of metal NPs in these cases. Moreover, it is difficult for the conventional photocatalysis to control the crystallographic orientation of metal NPs thus produced, which in turn determines the properties of metal NPs in many cases. In comparison to transition metals, the synthesis of main group metal NPs is less studied. Particularly, the synthesis of main group metal NPs by photochemical approach has not yet been reported.

Bismuth (Bi) is one of the most studied elements in solid-state physics because of its unusually rich electronic properties due to its complex and highly anisotropic Fermic surface.[7] A number of recent results, such as exotic electronic phenomena,[8] thermoelectricity,[9] and superconductivity,[10] are making Bi an interesting object of experimental and theoretical studies. Recently, considerable attention has been directed to nanostructured Bi because it may exhibit performance superior to its bulk counterpart.[9−11] It has been found that Bi NPs could act as the best catalysts for the growth of dimension-controlled semiconductor quantum wires and rods by the solution−liquid−solid mechanism.[12] A variety of methods, such as inverse micelles,[13] radiolytic reduction in aqueous solution,[14] the thermolysis of a bismuth-thiolate precursor,[15] and solution-

Received: January 8, 2013
Revised: April 23, 2013
Published: April 25, 2013

dx.doi.org/10.1021/cm400065x | *Chem. Mater.* 2013, 25, 2045−2050

based reduction,[16] have been thereby developed for the synthesis of Bi NPs. However, in situ reducing Bi-based oxide to achieve oriented growth of Bi NPs on a substrate has not yet been reported.[17] Controlling materials at the nanometer scale is of great challenge, particularly when long-range ordering is pursued.[18]

In the present work, we demonstrate a light-induced approach that couples the synthesis and oriented arrangement of Bi NPs without using organic agents via an in situ topotactic transformation process, in which $SrBi_2Ta_2O_9$ acts as a physical substrate, chemical source, and crystallization 'catalyst'. Our findings not only enrich the growth mechanisms for hybrid metal-semiconductor nanostructures but also prove that bulk metal oxide can be topotactically reduced to metal NPs with unique structures by a photochemical approach at ambient temperature.

EXPERIMENTAL SECTION

Sample Preparation. In this study, $SrBi_2Ta_2O_9$ (SBT) has been synthesized by a molten salt route.[19] In a typical synthesis, carbonates ($Sr(NO_3)_2$, 99%) and oxides (Bi_2O_3, and Ta_2O_5, 99.9%) were used as starting materials in a desired molar ratio, and NaCl and KCl were weighted by molar ratio of 1:1 as a mixed solvent. The raw materials and mixed solvent (in weight ratio 1:1) were ground for 0.5 h in an agate mortar. The mixture was first placed in an alumina crucible and heated in a tube furnace at 850 °C for 3 h and, subsequently, cooled naturally to room temperature. Pure $SrBi_2Ta_2O_9$ powder was obtained after removing the salt flux with deionized water and drying at 50 °C for 3 h.

Characterization. Powder X-ray diffraction (XRD) patterns were acquired using a Bruker D8 powder diffractometer with Cu Kα radiation, 0.02 step size, and 0.2 s step time. Thermogravimetry (TG) was performed on a NETZSCH STA 449F3 instrument. The sample was heated in an alumina crucible under air flow with a heating rate of 10 °C/min. Field emission scanning electron microscopy (FESEM) images were obtained on a ZEISS SUPRA55VP microscope. Transmission electron microscopy (TEM) was performed on JEOL model JEM-1210 and FEI Tecnai F30 electron microscopes at the accelerating voltage of 200 kV. The FEI Tecnai F30 was equipped for energy-dispersive X-ray spectroscopy. Optical properties were analyzed with a spectrophotometer (Shimadzu SolidSpec-3700DUV) and converted from reflection to absorbance by the standard Kubelka–Munk method. The nitrogen adsorption/desorption isotherms were acquired by a Micromeritics ASAP2020 sorptometer at −196 °C. Average pore diameters were determined using the Barrett–Joyner–Halenda (BJH) method.

Photochemical Reactions. Photoreaction was performed at 25 °C under atmospheric pressure in a closed circulation system using a high-pressure Hg lamp (500 W). A water filter was used to remove infrared light. SBT powder (0.2 g) was dispersed and magnetically stirred in a Pyrex top-irradiation reaction cell containing 90 mL H_2O and 15g $C_6H_{12}O_6{\cdot}H_2O$. The suspension was evacuated prior to irradiation and was maintained at about 25 °C by immersing the reaction cell in a water bath with a constantly controlled temperature. The produced H_2 and CO_2 were quantitatively measured by online gas chromatography (Agilent 7890A) with a thermal conductivity detector (TCD) and 5 Å molecular sieve column, using N_2 as carrier gas. Apparent quantum yield (A.Q.Y.) was calculated by the following equation: A.Q.Y. (%) = $N_e/N_p = 3N_{Bi}/N_p$, where N_p, N_e, and N_{Bi} represent the number of incident photons, the number of reacted electrons, and the number of reduced Bi atoms, respectively. The amount of the elemental Bi was determined by the weight loss on TG curve between 445 and 700 °C. The intensity of incident light was measured by a light flux meter (1930-C, Newport) with a light sensor. The average illumination intensity of the incident light at 365 nm (λ = 365 nm, half width = 15 nm) was 35 mW/cm^2.

RESULTS AND DISCUSSION

Light-Induced Color and XRD Changes of SBT. $SrBi_2Ta_2O_9$ (SBT) has proven to be a highly active photocatalyst under UV irradiation,[20] consistent with its band gap of 3.6 eV as estimated from the optical absorption onset (Figure S1, Supporting Information). Figure 1 shows the color change

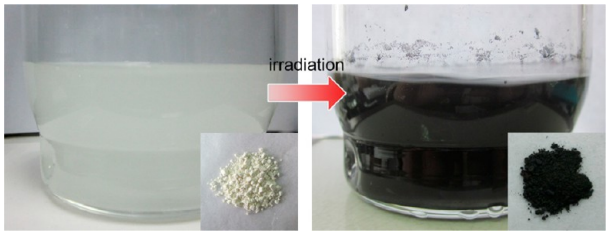

Figure 1. Photographs showing color change of SBT powders dispersed in aqueous glucose solution before and after photoreaction under UV light irradiation. The insets show the appearance of dried powders isolated from the Pyrex reaction cell.

of the $SrBi_2Ta_2O_9$ powder after 20 h of UV light irradiation. Surprisingly, the color of the powder changed from light yellow to distinct black, characteristic of significant chemical change of the materials.

Figure 2 shows the X-ray diffraction (XRD) patterns of SBT powers before and after the photocatalytic reaction. The main

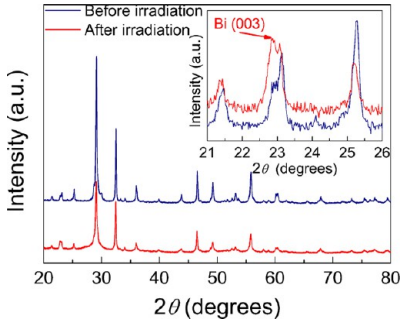

Figure 2. XRD patterns of SBT sample before and after photoreaction. The inset is the zoom-in of the XRD patterns from 21° to 26°.

diffraction peaks of both samples can be assigned to the structure of SBT. However, a new peak (marked by the arrows) at $2\theta \approx 22.7°$ appears after UV irradiation, which matches the (003) peak of rhombohedral Bi (JCPDS card no. 05-0519). Consequently, it is speculated that elemental Bi is formed from the photoreduction of SBT, and formation of this metal phase causes the color of SBT change from pale yellow to black as shown in Figure 1.

Morphological and Microstructural Features of Bi on SBT. Comparing parts a and b of Figure 3, the representative field emission scanning electron microscopy (FESEM) images of the samples before and after photoreaction, the original platelet shape of SBT retains even after 20 h photoreaction. The remarkable difference between the two samples is that the photogenerated Bi NPs are densely dispersed on the surface of the platelet, forming an adlayer-like pattern. In contrast, as shown in Figure 3a, the outer surface of SBT platelet before photoreaction appears smooth and no NPs. The FESEM result agrees with the transmission electron microscopy (TEM) analysis (Figure 3c and d and Figure S2, Supporting Information). The TEM image in Figure 3d shows that the

dx.doi.org/10.1021/cm400065x | Chem. Mater. 2013, 25, 2045−2050

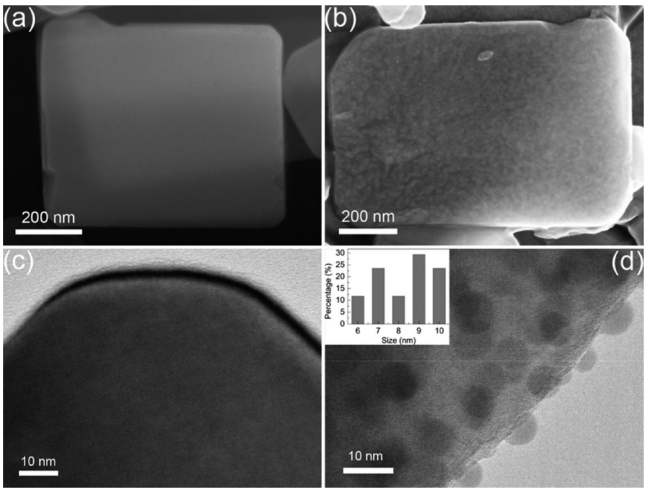

Figure 3. FESEM images and TEM images of SBT sample before (a, c) and after photoreaction (b, d). The inset in part d shows the histogram of particle size distribution.

diameter of the NPs located at the surface of the platelet is in the range of 6−10 nm. Corresponding particle size distribution histogram is shown in the inset. Therefore, it is concluded that the formation of this granular layer was due to the photoreaction at the surface of SBT in the presence of aqueous glucose.

Time-dependent evolution of the NP growth was also studied by TEM (Figure 4). At the initial stage (10 h), NPs

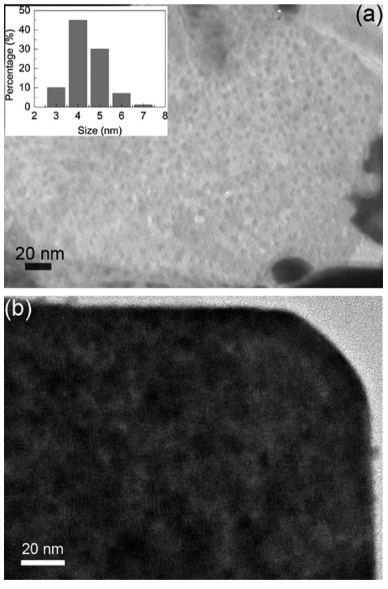

Figure 4. TEM images of SBT samples for (a) 10 h and (b) 30 h photoreaction. The inset of part a shows size distribution histogram.

with diameter of 3−7 nm and relatively low density were formed. The corresponding histogram inset in Figure 4a shows that the average particle diameter is 4.1 nm. As the phtotoreaction proceeded for 30 h, NPs with multiple sizes and shapes were formed on the top surface of SBT platelet because of the contacting among the NPs (Figure 4b). The coalescence of the NPs resulted in the large increase in particle sizes compared to the NPs obtained in 20 h. Therefore, it is concluded that the size of the NPs formed on the SBT platelet significantly increased with irradiation time, indicating the time-dependent growth of the particles with the photoreaction.

Figure 5a shows the high-resolution TEM (HRTEM) image of a single NP anchored to the edge of the SBT platelet (after

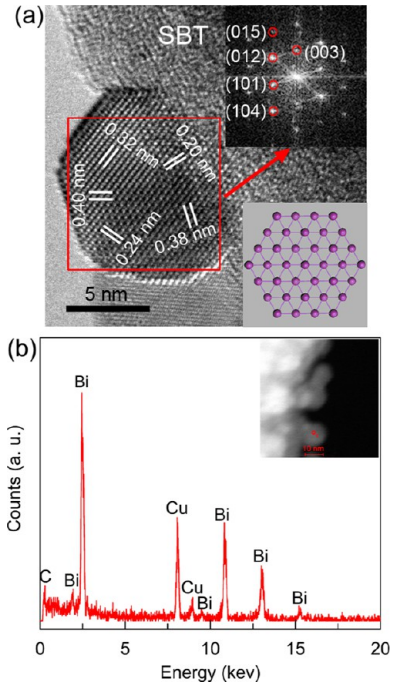

Figure 5. (a) HRTEM images of a single NP anchored to the SBT edge. The insets of part a are the corresponding FFT of the region as marked by the red square and a schematic atomic structure of NP. (b) EDX spectrum of a single NP anchored to the SBT edge acquired from the red circled region in HAADF-STEM image of Bi-SBT (inset of part b).

20 h of photoreaction). The fast Fourier transformation (FFT) of the TEM image shows a pattern of 5 spots corresponding to the crystallographic planes of rhombohedral Bi. Additional representative HRTEM images are presented in Figure S3, Supporting Information. Figure 5b gives the high angle annular dark field scanning TEM (HAADF-STEM) image and a representative EDX spectrum recorded from the individual NPs anchored to the edge of the platelet, further confirming the formation of elemental Bi product. The carbon and copper signals originate from the carbon-coated copper grid. More EDX investigation on other NPs anchored to the edge also proves that bismuth is the only detectable element (Figure S4, Supporting Information).

It is reasonable to speculate that the NPs formed on the top of platelet are also metallic Bi because no other new peaks are observed in the XRD patterns (Figure 2) except that of Bi (003). Measuring the NPs on the surface of SBT by EDX, four elements, Sr, Bi, Ta, and O are detected (Figure S5, Supporting Information). Due to the interference by the SBT substrate, the composition of the NPs cannot be exclusively identified in this way. To further prove that the surface NPs are only composed of elemental Bi, the sample after photoreaction was quickly heated from room temperature up to 500 °C with a heating rate of 25 °C min^{-1} and annealed at 500 °C for 1 h in air. After such thermal treatment, the sample color turns back to light yellow (almost identical to the original color of pristine SBT, Figure 6a), indicating disappearance of metallic Bi, which has proven

dx.doi.org/10.1021/cm400065x | *Chem. Mater.* 2013, 25, 2045−2050

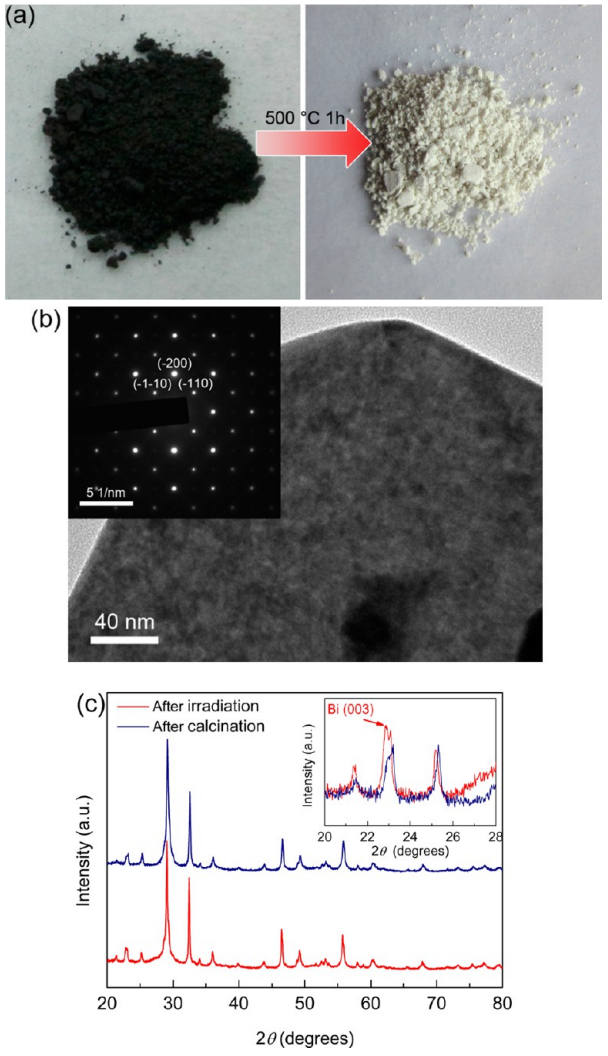

Figure 6. (a) Color and (c) XRD changes of the irradiated sample before and after calcination. (b) TEM image of SBT after calcination. The inset of part b is the corresponding SAED pattern.

to be easily vaporized at 500 °C.[21] The vaporization of Bi is also supported by the selected area electron diffraction (SAED) pattern (Figure 6b) and the disappearance of the XRD peak at $2\theta \approx 22.7°$ (Figure 6c) of the sample after thermal treatment.

The vaporization of Bi NPs leaves mesopores on the top of the platelet as clearly proved by black spots in FESEM images (Figure S6, Supporting Information) and N_2 adsorption (giving a narrow distribution of the pores at ~3.8 nm, Figure S7, Supporting Information). These observations are consistent with the results of thermogravimetry (TG) (Figure S8, Supporting Information), which shows a relatively high-temperature weight loss by about 2% of its initial weight between 445 and 700 °C. Considering the fact that the metal oxides within SBT are not evaporable at 500 °C (because the SBT can be synthesized at 850 °C), the above observed morphology change and weight loss at elevated temperature is solely due to the vaporization of metallic Bi. This means that the NPs formed on the top of SBT platelet are composed of elemental Bi. Without light irradiation, no NPs were ever observed on the surface of SBT (Figure S9, Supporting Information), even after placing it in a glucose solution for long time (20 h), indicating that the reduction of Bi(III) in SBT is due to photochemical process.

To further investigate the role of glucose in the growth of Bi NPs, the control experiment without glucose was also carried out under identical conditions, in which hydrogen evolution was hardly observed. The XRD pattern and FESEM image of SBT powers after photoreaction for 20 h in the absence of glucose are provided in the Supporting Information (Figure S10). The XRD pattern of the catalyst after the reaction is not affected by photoreaction and the (003) peak of rhombohedral Bi is hardly visible. Additionally, no NPs were found on the SBT platelet after photoreaction. These results indicate that the presence of glucose indeed plays a key role in the process of Bi NP growth.

HRTEM image taken from the top surface of SBT platelet after 20 h photoreaction is shown in Figure 7a1, where distinct

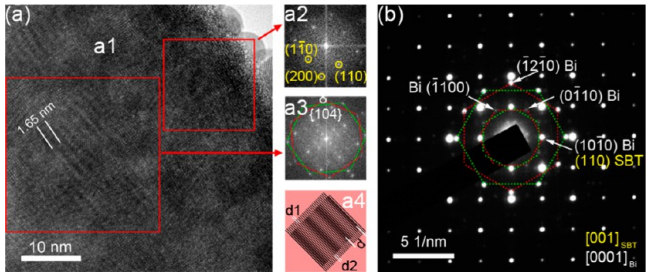

Figure 7. (a) HRTEM image taken from the top surface of SBT platelet after 20 h photoreaction. FFT patterns (a2, a3) corresponding to the areas marked by red square. (a4) Schematic illustration of the Moiré fringes in (a1). The lines in this figure represent the lattice planes in the crystals. (b) SAED pattern measured over the atop Bi NPs along the $[0001]_{Bi}$ and $[001]_{SBT}$ zone axis. Two sets of SAED spots corresponding to the rhombohedral Bi are marked by red and green dashed lines.

Moiré fringes are observed, which are formed from the interference of two relaxed crystal lattices. The spacing (d) of the Moiré fringes is determined to be 1.68 nm according to eq 1:[22]

$$d = \frac{d1 \times d2}{|d1 - d2|} \quad (1)$$

where d1 (0.24 nm) and d2 (0.21 nm) are the interplanar spacings for the Bi {104} and SBT {220} planes, respectively. This d value is identical within experimental error to the observed value of 1.65 nm (Figure 7a1). The FFT pattern of two domains marked in Figure 7a1 corresponds to the pure SBT substrate (yellow circles, Figure 7a2) and a combination of SBT substrate and Bi NPs (white circle, Figure 7a3), respectively. For the substrate SBT, single-crystalline characteristic is confirmed by the SAED pattern (Figure 7b and Figure S2c, Suporting Information). On the other hand, the SAED pattern measured over the atop Bi NPs along the $[0001]_{Bi}$ zone axis (Figure 7b) shows that, in addition to the spots due to SBT, two sets of extra diffraction spots (marked by red and green lines) indexed well to the rhombohedral Bi are simultaneously observed, suggesting that the primary Bi crystals have two sets of in-plane orientations. This observation indicates that the overall crystalline aggregates are long-range ordered although the positioning of individual NPs within a local area seems to be random.[23] This highly organized arrangement of Bi NPs is analogous to the previously observed NP assembly in mesocrystals, in which the elemental units are nanocrystals that all grow in the same crystallographic

dx.doi.org/10.1021/cm400065x | Chem. Mater. 2013, 25, 2045−2050

orientation in a manner of single crystal.[23] Mesocrystals are of strong interest, mainly due to their new chemical and physical properties compared to the individual nanocrystals.[24] Considering the unique features of Bi metal, the surface supported mesocrystal-like Bi assemblies will be of great interest for fundamental physics and chemistry studies, where some unprecedented properties are expected to emerge from the anisotropic nature.

Mechanism of the Photochemical Topology Process. The formation mechanism of the Bi NPs is schematically illustrated in Figure 8, which is closely related to the crystal

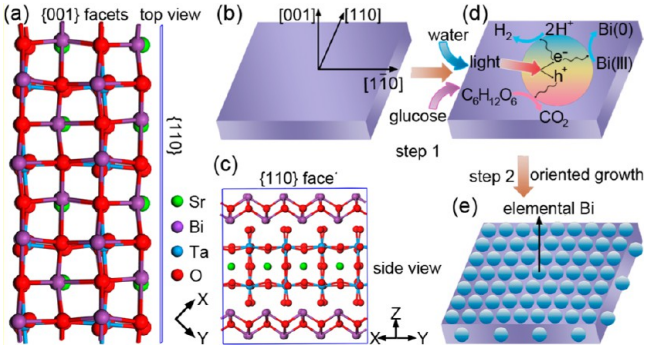

Figure 8. Schematic crystal structure and stacking models of SBT. Top (a) and side (b) views of surface structures of the SBT platelet, respectively. (c) Schematic illustration of the crystal orientation of the SBT platelet. (d, e) Formation mechanism of the oriented Bi NPs from SBT via a topotactic photochemical transformation reaction under light irradiation.

structure of SBT, and can be described as an intergrowth between $(Bi_2O_2)^{2+}$ sheets and $(SrTa_2O_7)^{2-}$ perovskite like layers (Figure 8a, b). According to the results in Figure 7 and the symmetries of SBT, the bottom and top surfaces of the SBT platelet are terminated {001} facets, while the side surfaces are {110} facets. The atomic structures of the {001} and {110} facets are shown in Figure 8a and b, respectively. Under photochemical conditions, some photogenerated electrons in {110}-oriented SBT platelets are trapped by the $(Bi_2O_2)^{2+}$ terminated {001} surface because these planes have a net of positive charges,[25] resulting in the formation of Bi atoms via a topotactic reduction process (step 1 in Figure 8) similar to the topotactic electroreduction procedure.[26] The photogenerated electrons also act as reducing agents to convert protons to H_2, whereas the photogenerated holes are simultaneously consumed by glucose to eventually convert to CO_2. This unique process results in much higher ratio of CO_2/H_2 than that of the stoichiometric photoreforming reaction of glucose,[27] in agreement with the experimental observations. As shown in Figure 9, in the present system, the evolved gas analysis indicates the production of CO_2 and H_2 during photoreaction, and their ratio is ~1.1/1 after 20 h of photoreaction, respectively. This CO_2/H_2 ratio is significantly higher than that of the stoichiometry of the photoreforming reaction of glucose.[27] The apparent quantum yield of SBT sample at 365 nm is calculated to be 0.066%.

Because of the cryalline lattice match between $(110)_{SBT}$ and $(003)_{Bi}$ planes (both having d spacing ≈0.4 nm), the in situ photoreduction of Bi(III) results in oriented nucleation of Bi from the $(003)_{Bi}$ plane via in situ topotactic transformation. These nuclei serve as seeds for continuous NPs growth with the epitaxial relationship of $[001]_{Bi}//[110]_{SBT}$ as more Bi atoms are

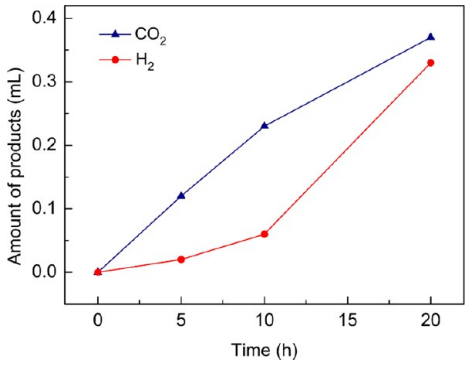

Figure 9. CO_2 and H_2 evolutions from photochemical decomposition of $C_6H_{12}O_6$ over SBT under UV light irradiation.

transferred from bulk to surface by diffusion (step 2 in Figure 8). The oriented nuclei are developed preferentially along the two perpendicular [110] and [1$\bar{1}$0] directions within the SBT platelet plane, resulting in two sets of in-plane orientations of the Bi NPs, as indeed evidenced in the SAED spots in Figure 7b. The driving force for the diffusion process might result from the concentration gradient of the reduced Bi atoms constrained in the SBT particles. Similar behavior has also been reported in the literature for Bi NPs growth.[28] With this diffusion process, the chemical potential and interface energy of entire system will be decreased. The outward diffusions of both Bi and O^{2-}lead to the formation of voids within the SBT domains as is proved by the FESEM images (Figure S6, Supporting Information) and pore size distributions (Figure S7, Supporting Information) of the annealed Bi-SBT, which is similar to the electroreduction procedure.[29] A similar crystal growth process has previously been observed in galvanic replacement reactions.[30] The formation of Bi NPs on the edge of SBT platelet is likely caused by a defect growth mechanism.

Along with the crystal structure, the band positions of SBT with respect to the electrode potential of $(Bi_2O_2)^{2+}/Bi$ are equally important. For the growth of Bi NPs, the conduction band level of SBT should be more negative than the reduction potential of $(Bi_2O_2)^{2+}$ to form Bi. First principal calculations reveal that the conduction band minimum (CBM) of SBT is mainly determined by Ta 5d state, which has higher reduction potential than most other d^0 elements.[20,31] Under UV light irradiation, the excited electrons in the CB of SBT possess a high enough reduction potential to reduce $(Bi_2O_2)^{2+}$ in SBT. Therefore, the reduction potential of SBT might be one of the factors for the Bi NPs growth. Theoretically, for semiconductors in aqueous solution, the photogenerated electrons in the conduction band can reduce the cations therein depending on thermodynamic and kinetic conditions.[32] According to the work by Chen and coauthors,[32] all the semiconductors that satisfies the conditions are likely susceptible to be reduced. Except for the photoinduced growth of Bi NPs from SBT, Ag^+ ions in Ag_2CO_3 were also found to be reduced to form metallic Ag as reported by Yu et al.[33]

Substrate supported metal NPs offer an important class of nanomaterials due to their tunable size and interfacial interaction. However, most of metal NPs are synthesized in liquid phase and must be coated with organic capping ligands to prevent aggregation and phase transformation into bulk phase. These capping ligands often significantly interfere the interfacial interaction between the NPs and substrate.[34] The in situ photoreduction method developed in this study enables

dx.doi.org/10.1021/cm400065x | Chem. Mater. 2013, 25, 2045−2050

ligand-free fabrication of monodispersed metal NPs, which are stabilized by the strong epitaxial interaction between the metal and metal oxide phase (as shown in Figure 7). Such clean nanostructures may offer new material systems for systematic investigation and improvement of the catalytic performance. Further study exploring the application of the supported Bi NPs is currently underway.

CONCLUSIONS

In summary, this work presents a novel approach to fabricate surface supported Bi NPs by in situ topotactic photoreduction of SBT. Our findings prove that bulk metal oxide can be photoreduced under ambient condition to produce well-defined nanocrystals. This newly developed method has several features regarding nanomaterials fabrication and potential application in surface science and catalysis: (i) producing Bi NPs homogeneously distributed onto the entire surface of SBT platelet; (ii) achieving large area crystallographic alignment of Bi NPs, which is otherwise very difficult to achieve by other methods; (iii) producing epitaxial interface between Bi and SBT phase, which enables strong electronic communicatin between the two phases when used in catalysis; and (iv) being simple and environmentally friendly in view of the direct photoreduction of metal oxide to metal under ambient condition.

ASSOCIATED CONTENT

Supporting Information

Experimental details, UV−vis spectrum, additional TEM and SEM images, EDX spectrum, N_2 adsorption−desorption isotherms and pore size distributions, and TG analysis. This material is available free of charge via the Internet at http://pubs.acs.org.

AUTHOR INFORMATION

Corresponding Author

*E-mail: yxli@ms.xjb.ac.cn (Y.L.); cywang@ms.xjb.ac.cn (C.W.).

Notes

The authors declare no competing financial interest.

ACKNOWLEDGMENTS

This work was supported by the National Nature Science Foundation of China (Grant Nos. 21001113, 21173261), the "One Hundred Talents Project Foundation Program" of Chinese Academy of Sciences, International Science and Technology Cooperation Program of Xinjiang Uygur Autonomous Region (20116010), the "Cross-Cooperation Program for Creative Research Teams" of Chinese Academy of Sciences, and the "Western Light" Program of Chinese Academy of Sciences (XBBS200916).

REFERENCES

(1) Xia, Y.; Xiong, Y.; Lim, B.; Skrabalak, S. E. *Angew. Chem., Int. Ed.* **2009**, *48*, 60.
(2) Cölfen, H.; Mann, S. *Angew. Chem., Int. Ed.* **2003**, *42*, 2350.
(3) Oyelaran, O.; Novet, T.; Johnson, C. D.; Johnson, D. C. *J. Am. Chem. Soc.* **1996**, *118*, 2422.
(4) Han, W.-K.; Choi, J.-W.; Hwang, G.-H.; Hong, S.-J.; Lee, J.-S.; Kang, S.-G. *Appl. Surf. Sci.* **2006**, *252*, 2832.
(5) Fujishim, A.; Honda, K. *Nature* **1972**, *238*, 37.
(6) (a) Li, J.; Xu, J.; Dai, W.-L.; Fan, K. *J. Phys. Chem. C* **2009**, *113*, 8343. (b) Hidalgo, M. C.; Maicu, M.; Navío, J. A.; Colón, G. *J. Phys. Chem. C* **2009**, *113*, 12840. (c) Zhang, J.; Li, L.; Yan, T.; Li, G. *J. Phys. Chem. C* **2011**, *115*, 13820.
(7) Marcano, N.; Sangiao, S.; Magén, C.; Morellón, L.; Ibarra, M. R.; Plaza, M.; Pérez, L.; Teresa, J. M. D. *Phys. Rev. B* **2010**, *82*, 125326.
(8) (a) Behnia, K.; Balicas, L.; Kopelevich, Y. *Science* **2007**, *317*, 1729. (b) Li, L.; Checkelsky, J. G.; Hor, Y. S.; Uher, C.; Hebard, A. F.; Cava, R. J.; Ong, N. P. *Science* **2008**, *321*, 547.
(9) Heremans, J. P.; Thrush, C. M.; Morelli, D. T.; Wu, M.-C. *Phys. Rev. Lett.* **2002**, *88*, 216801.
(10) Tian, M.; Wang, J.; Kumar, N.; Han, T.; Kobayashi, Y.; Liu, Y.; Mallouk, T. E.; Chan, M. H. W. *Nano Lett.* **2006**, *6*, 2773.
(11) Lee, K.; Lee, S.; Holmes, S. N.; Ham, J.; Lee, W.; Barnes, C. H. W. *Phys. Rev. B* **2010**, *82*, 245310.
(12) (a) Yu, H.; Li, J.; Loomis, R. A.; Gibbons, O. C.; Wang, L.-W.; Buhro, W. E. *J. Am. Chem. Soc.* **2003**, *125*, 16168. (b) Dong, A.; Wang, F.; Daulton, T. L.; Buhro, W. E. *Nano Lett.* **2007**, *7*, 1308. (c) Dong, A.; Tang, R.; Buhro, W. E. *J. Am. Chem. Soc.* **2007**, *129*, 12254. (d) Wang, F.; Yu, H.; Li, J.; Hang, Q.; Zemlyanov, D.; Gibbons, P. C.; Wang, L.-W.; Janes, D. B.; Buhro, W. E. *J. Am. Chem. Soc.* **2007**, *129*, 14327. (e) Wang, F.; Buhro, W. E. *J. Am. Chem. Soc.* **2007**, *129*, 14381. (f) Wang, F.; Tang, R.; Yu, H.; Gibbons, P. C; Buhro, W. E. *Chem. Mater.* **2008**, *20*, 3656.
(13) Foos, E. E.; Stroud, R. M.; Berry, A. D.; Snow, A. W.; Armistead, J. P. *J. Am. Chem. Soc.* **2000**, *122*, 7114.
(14) Gutierrez, M.; Henglein, A. *J. Phys. Chem.* **1996**, *100*, 7656.
(15) Wang, Y.; Chen, J.; Chen, L.; Chen, Y.-B.; Wu, L.-M. *Cryst. Growth Des.* **2010**, *10*, 1578.
(16) Wang, Y. W.; Hong, B. H.; Kim, K. S. *J. Phys. Chem. B* **2005**, *109*, 7067.
(17) Li, Y.; Wang, J.; Deng, Z.; Wu, Y.; Sun, X.; Yu, D.; Yang, P. *J. Am. Chem. Soc.* **2001**, *123*, 9904.
(18) Yuan, B.; Xing, L.-L.; Zhang, Y.-D.; Lu, Y.; Mai, Z.-H.; Li, M. *J. Am. Chem. Soc.* **2007**, *129*, 11332.
(19) Song, Y.-X.; Li, C.-E.; Yan, H.-X. *J. Inorg. Mater.* **2002**, *17*, 145.
(20) Li, Y.; Chen, G.; Zhang, J.; Li, Z. *J. Solid State Chem.* **2008**, *181*, 2653.
(21) Li, L.; Yang, Y.-W.; Li, G.-H.; Zhang, L.-D. *Small* **2006**, *2*, 548.
(22) Sayed, S. Y.; Wang, F.; Malac, M.; Meldrum, A.; Egerton, R. F.; Buriak, J. M. *ACS Nano* **2011**, *3*, 2809.
(23) Xu, A.-W.; Antonietti, M.; Yu, S.-H.; Cölfen, H. *Adv. Mater.* **2008**, *20*, 1333.
(24) (a) Tartaj, P.; Amarilla, J. M. *Adv. Mater.* **2011**, *23*, 4904. (b) Cölfen, H.; Meldrum, F. *Chem. Rev.* **2008**, *108*, 4332. (c) Song, R.-Q.; Cölfen, H. *Adv. Mater.* **2010**, *22*, 1301.
(25) Paz de Araujo, C. A.; Cuchiaro, J. D.; McMillan, L. D.; Scott, M.; Scott, J. F. *Nature* **1995**, *374*, 627.
(26) He, Z.; Gudavarthy, R. V.; Koza, A. J.; Switzer, J. A. *J. Am. Chem. Soc.* **2011**, *133*, 12358.
(27) Tomoji, K.; Tadayoshi, S. *Nature* **1980**, *286*, 474.
(28) Chen, J.; Wu, L.-M.; Chen, L. *Inorg. Chem.* **2007**, *46*, 586.
(29) Li, W.; Jin, X.; Huang, F.; Chen, G. Z. *Angew. Chem., Int. Ed.* **2010**, *49*, 3203.
(30) (a) Sun, Y.; Xia, Y. *J. Am. Chem. Soc.* **2004**, *126*, 3892. (b) Liu, Y.; Walker, A. R. H. *ACS Nano* **2011**, *5*, 6843.
(31) Mukherji, A.; Seger, B.; Lu, G. Q.; Wang, L. *ACS Nano* **2011**, *5*, 3483.
(32) Chen, S.; Wang, L.-W. *Chem. Mater.* **2012**, *24*, 3659.
(33) Dai, G.; Yu, J.; Liu, G. *J. Phys. Chem. C* **2012**, *116*, 15519.
(34) Xi, G.; Ye, J.; Ma, Q.; Su, N.; Bai, H.; Wang, C. *J. Am. Chem. Soc.* **2012**, *134*, 6508.